Circadian rhythms and the light-dark cycle interact to regulate amyloid plaque accumulation and tau phosphorylation in 5xFAD mice.

Melvin W. King[1], Sophie Jacob[1], Ashish Sharma[1], Jennifer H. Lawrence[1], David R. Weaver[2], Erik S. Musiek[1,*]

[1]Department of Neurology & Center On Biological Rhythms & Sleep, Washington University School of Medicine in St. Louis, St. Louis, MO, USA

[2]Department of Neurobiology, UMass Chan Medical School, 366 Plantation Street, NERB, Worcester MA, USA

*Address Correspondence to: Erik S. Musiek, MD, PhD, Dept. of Neurology, Washington University School of Medicine, Campus Box 8111, 425 S. Euclid Ave., St. Louis, MO, 63110. musiek@wustl.edu

Keywords: circadian rhythms, Alzheimer's Disease, amyloid, suprachiasmatic nucleus, tau

Abstract

Background

Circadian disruption has long been appreciated as a downstream consequence of Alzheimer's Disease in humans. However, an upstream role for behavioral circadian disruption in regulating AD pathology remains an open question.

Methods

To determine the role of the central circadian clock in the suprachiasmatic nucleus (SCN) in regulating amyloid pathology, we crossed the 5xFAD amyloid mouse model with mice harboring deletion of the critical clock gene *Bmal1* in GABAergic neurons using VGAT-iCre, which is expressed in >95% of SCN cells. To examine the role the light-dark cycle in this process, we aged these mice in either regular 12:12 light-dark (LD) or constant darkness (DD) conditions. Transcriptional, behavioral, and physiological rhythms were examined in VGAT-iCre; 5xFAD; *Bmal1*$^{fl/fl}$ (VGAT-BMAL1KO;5xFAD) mice under varying light conditions. Amyloid plaque deposition, peri-plaque tau phosphorylation, and other pathology was examined by immunohistochemistry, and transcriptomic changes were examined by high-throughput qPCR.

Results

VGAT-BMAL1KO;5xFAD mice showed loss of SCN BMAL1 expression and severe disruption of behavioral rhythms in both LD and DD, with loss of day-night rhythms in consolidated sleep and blunting of rhythmic clock gene expression in the brain. Surprisingly, VGAT-BMAL1KO;5xFAD mice kept under LD showed reduced total plaque accumulation and peri-plaque tau phosphorylation, compared to Cre-negative controls. These changes were gated by the light-dark cycle, as they were absent in VGAT-BMAL1KO;5xFAD mice kept in DD conditions. Total plaque accumulation was also reduced in control 5xFAD mice kept in DD as compared to LD, suggesting a general effect of light-dark cycle on amyloid aggregation. Expression of murine presenilin 1 (Psen1) -- which catalyzes the processing of sAPPβ into Aβ -- as well as APP cleavage to C-terminal fragments, were suppressed in VGAT-BMAL1KO;5xFAD under LD conditions.

Conclusions

These studies elucidated an interaction between the circadian clock in GABAergic neurons and the light-dark cycle in regulating amyloid pathology and suggest that decoupling the central clock form the light-dark cycle may reduce APP cleavage and plaque formation. These results call into question the proposed simple positive feedback loop between circadian rhythm disruption and Alzheimer's Disease pathology.

Introduction

Alzheimer's Disease is a progressive, debilitating neurological disorder that effects nearly 6.9 million people aged 65 or over and is the leading cause of dementia in the United States [1]. Disruption of endogenous circadian and sleep rhythms has long been appreciated as a downstream consequence of Alzheimer's Disease [2,3]. However, an upstream role for circadian disruption in AD progression -- and in particular the aggregation of Aβ plaques -- has yet to be defined [4]. Evidence consistent with a causal role for circadian disruption comes from numerous human studies demonstrating transcriptional and behavioral circadian abnormalities as a function of age, the primary risk factor for developing AD [5,6]. The presence of preclinical Aβ or tau pathology in cognitively normal individuals has been associated with increased circadian fragmentation, suggesting that circadian dysfunction occurs very early in the disease course [7]. Given the pervasiveness of the circadian system at various levels of biology, how these disruptions contribute to the initiation and progression of AD pathology is a significant unknown.

A few previous studies have examined the impact of circadian disruption on AD pathology in mouse models using genetic ablation of the transcription factor Bmal1 (aka *Arntl*), as BMAL1 protein dimerizes with CLOCK or NPAS2 to drive cellular rhythms through the core circadian Transcriptional-Translation Feedback Loop (TTFL) [8,9]. Inducible whole-body knockout of *Bmal1* causes behavioral arrhythmicity in mice and exacerbates hippocampal plaque pathology in the APP/PS1-21 model of AD [10,11]. However, a suprachiasmatic nucleus (SCN)-sparing *Bmal1* deletion failed to have the same impact on plaque deposition [12]. This suggests that disrupting *Bmal1* across cell types may exert complicated circadian and non-circadian effects that impact amyloid dynamics. It remains unknown whether specifically disrupting rhythmic output from the SCN, which coordinates brain- and body-wide rhythms by a combination of synaptic and hormonal cues and whose rhythmic output degrades with age, may influence Aϐ plaque pathology [13,14].

One classic strategy for disrupting SCN function is through mechanical ablation. However, the SCN is small and surrounded by dozens of other critical hypothalamic nuclei which may be variably damaged in this process, exerting unknown effects. Thus, a genetic approach is preferable. Since more than 95% of SCN neurons are GABAergic, targeted deletion of *Bmal1* in GABAergic neurons the using VGAT-ires-Cre produces mice which are behaviorally arrhythmic in constant darkness (DD) [15,16]. It is unknown how this restricted *Bmal1* deletion impacts amyloid pathology in mice. However, mice with a genetically ablated clock do maintain some rhythmic behavior under regular light-dark lighting cycles due to phenomenon called masking, and the effect of this on amyloid pathology is also unknown [17,18].

Here, we have examined the effect of GABAergic *Bmal1* deletion on circadian function and amyloid-related pathology in 5xFAD mouse model of amyloid pathology[19]. We performed experiments with VGAT-iCre; *Bmal1*$^{fl/fl}$;5xFAD$^{+/-}$ mice (referred to as VGAT-BMAL1KO;5xFAD) and Cre- controls under both LD (in which Cre+ mice have some rhythmic behavior due to zeitgeber cues) and DD conditions (under which Cre+ mice are fully arrhythmic) to help isolate the potential effects of the light-dark cycle and

circadian rhythmicity from non-circadian effects of *Bmal1* deletion. To our surprise, we have found that disruption of behavioral and transcriptional rhythms via GABAergic *Bmal1* deletion caused a decrease in amyloid plaque accumulation and plaque-related tau phosphorylation, but only mice kept under LD conditions. That is, mice with a semblance of behavioral rhythm after knockout had ameliorated AD pathology, but pathology in mice with a total absence of circadian rhythms was unchanged. These studies suggest that specific interactions between the light-dark cycle and the molecular clock may drive changes in plaque pathology, and provoke a rethinking of proposed linear relationship between behavioral arrhythmicity and AD pathology.

Results

GABAergic *Bmal1* deletion disrupts circadian behavior in light-dark and constant darkness

Inhibitory GABAergic synaptic transmission is ubiquitous throughout the brain, so we first aimed to characterize the expression of VGAT-ires-Cre in various brain regions. We crossed VGAT-ires-Cre mice to a mouse line expressing tdTomato upstream of a *loxP*-flanked STOP cassette, enabling permanent labeling of VGAT-expressing cells [20]. We observed heavy tdTomato labeling within the suprachiasmatic nucleus and striatum (Figs 1A, S1A), in agreement with previous reports [21]. Intense tdTomato signal was noted in the striatum and basal ganglia (Fig. S1A), as most of these neurons are GABAergic, while only sparse labeling was seen within the medial cortex and hippocampus, with roughly 20% of NeuN+ expressing tdTomato across both regions (Fig. S1B).

Given the role of the suprachiasmatic nucleus and BMAL1 in maintaining organismal and cellular circadian rhythms, we then assessed the role of GABAergic *Bmal1* in regulating circadian behavior under light-dark and constant darkness. We crossed VGAT-ires-Cre to a *Bmal1*$^{fl/fl}$ line to generate Cre- controls and Cre+ VGAT-BMAL1KO mice and aged them to two months. Circadian activity was assessed with infrared actigraphy monitoring under LD (1 week) and DD (2 weeks) conditions. Under LD conditions, Cre+ mice showed some diurnal rhythms in activity but had noticeably dampened amplitude (Fig 1D,E), and had onset of their active phase nearly four hours earlier than Cre- mice, which normally become active at lights off (ZT12). Upon release into constant darkness, Cre- mice maintained circadian activity rhythms with an average period of 23.6 hours, while Cre+ mice immediately lost coherent rhythmic activity by periodogram analysis, with no detectable circadian period (Fig 1F, S1D). Post-mortem BMAL1 immunohistochemical (IHC) analysis confirmed the near total loss BMAL1 protein within the SCN (Fig 1B, 1C). Interestingly, despite intense tdTomato expression within the striatum, VGAT-Cre mediated excision only reduced BMAL1 protein expression within this region by roughly half, whereas total BMAL1 protein expression at the IHC level within the cortex and hippocampus was unaffected, suggesting that GABAergic interneurons are not major expressors of *Bmal1* in the cortex and

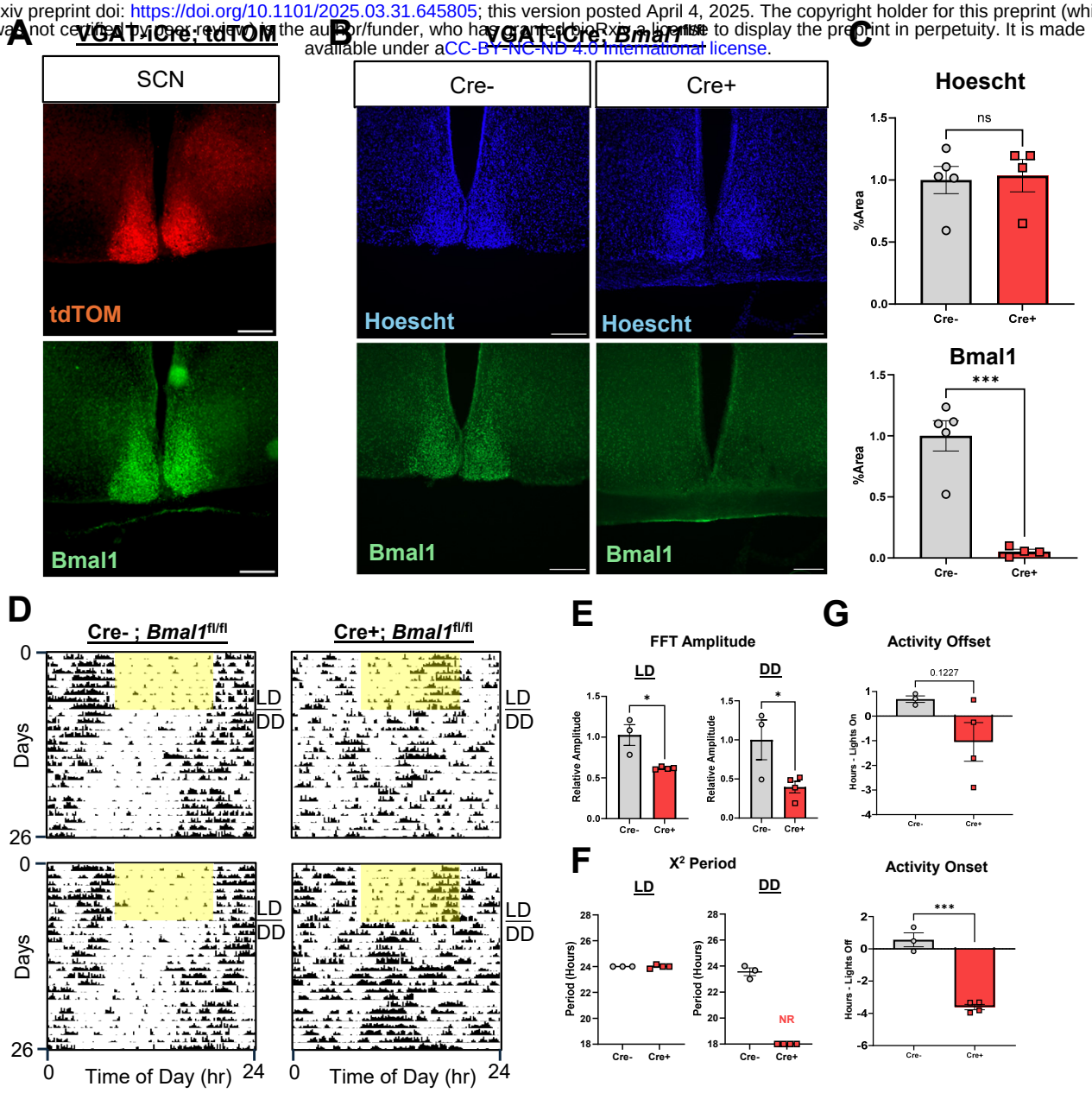

Figure 1. VGAT-*Bmal1* knockout disrupts circadian behavior in light-dark and constant darkness. **A.** Immunostaining of Bmal1 (green) with auto-fluorescent tdtomato (red) on SCN sections of *VGAT-ires-iCre;tdTOM lox-stop-lox* mice. Scale bars are 200 µm **B.** Double immunostaining of DAPI (blue) and Bmal1 (green) on SCN sections of *VGAT-ires-Cre;Bmal*$^{fl/fl}$ mice. Scale bars are 200 µm **C.** Quantification of staining from (B) (Cre+: VGAT-ires-iCre+ Bmal$^{fl/fl}$, n=5, Cre-: VGAT-ires-iCre- Bmal$^{fl/fl}$, n=4) values are mean +/- SE (*** Student's t, $p < 0.0005$) **D**. Representative actograms of *VGAT-ires-iCre;Bmal*$^{fl/f}$ mice. All mice were placed into 12:12 LD for at least transferred into DD, as indicated on the plot. Yellow bars represent days of LD -- hour 6 to hour 18. Cre+ mice became immediately arrythmic upon release into DD. **E.** Quantification of FFT Amplitude from actogram data plotted in (D). LD analysis was performed on data generated on days 2-9. DD analysis data was taken from days 12-19. *VGAT-ires-iCre+;Bmal*$^{fl/fl}$ DD mice exhibited low average amplitude in the circadian range compared to *VGAT-ires-iCre-;Bmal*$^{fl/fl}$ *control mice.* (n = 3-4 mice per genotype as indicated; *Student's t, $p < 0.05$) **F.** X^2 periodogram analysis from actogram data plotted in (D). LD period analysis was performed on data generated on days 2-9. DD analysis data was taken from days 12-19. *VGAT-ires-iCre+;Bmal*$^{fl/fl}$ DD mice exhibited no coherent rhythms (NR) compared to *VGAT-ires-iCre-;Bmal*$^{fl/fl}$ *control mice.* No period differences were seen between mice in LD. **G.** (Top) Average activity offset time (see methods) minus lights on time (ZT0 or hour 6). (Top) Average activity onset time minus lights off (ZT12 or hour 18) (n=3-4 mice per group as indicated *** Student's t, $p < 0.0005$).

hippocampus (Fig S1C). Collectively these results demonstrate the importance of GABAergic *Bmal1* in the maintenance of circadian behavior rhythms under light-dark, and its necessity in constant darkness.

GABAergic *Bmal1* excision disrupts sleep and transcriptional rhythms in 5xFAD mice

Our next goal was to explore how GABAergic BMAL1 influences rhythmic physiology in a mouse model of Alzheimer's Disease. We crossed 5xFAD mice, which harbor a human amyloid precursor protein (APP) with the Swedish (KM670/671NL), Florida (I716V), and London (V717I) mutations and human presenilin 1(PSEN1) with the M146L and L286V mutations, to the VGAT-ires-Cre;*Bmal1*$^{fl/fl}$ line to generate VGAT-iCre; *Bmal1*$^{fl/fl}$;5xFAD$^{+/-}$ mice (referred to as VGAT-BMAL1KO;5xFAD) and Cre-; *Bmal1*$^{fl/fl}$;5xFAD$^{+/-}$ controls [19]. Mice were aged in LD until 5 months, when substantial plaque development has taken place within the cortex and hippocampal regions. As before, while Cre+;5xFAD mice were able to entrain to a regular light-dark cycle, their circadian amplitude was negatively impacted compared to Cre-;5xFAD controls (Fig 2C, S2A). Constant darkness abrogated rhythms in 4/4 Cre+ mice by χ^2 periodogram analysis, demonstrating the efficacy of this paradigm in disrupting rhythms in 5xFAD mice in LD and DD.

We simultaneously measured sleep, a circadian controlled process whose disruption is associated with risk of dementia in humans, using piezoelectric monitoring [22,23]. Total sleep percentage over a 24-hour period was unchanged between Cre+ and Cre- 5xFAD mice. However, in accordance with their earlier onset time, Cre+ mice spent less time sleeping during the inactive or light phase, particularly from ZT6 to ZT12 (Fig 2E, 2F). By comparison, Cre+ spent a larger percentage of time sleeping during the dark phase, particularly between ZT14 and ZT18. Free-running behavior (Cre-) and circadian fragmentation (Cre+) prevented division of sleep behavior in DD into active and inactive epochs, but overall sleep amount remained the same between Cre- and Cre+ mice, similar to LD (Fig S2B). Despite significant circadian disruption between Cre- and Cre+ mice, the total amount of sleep, to which plaque deposition in mouse models is strongly sensitive, remained unchanged [24–26].

Finally, we examined the role of GABAergic BMAL1 in driving hippocampal transcriptional rhythms in these mice under light-dark. Bulk hippocampal tissue was harvested from VGAT-BMAL1KO;5xFAD mice across six times of day under LD, and analyzed with a panel of transcripts associated with circadian and clock function (Fig 2G). Because Cre+ mice are arrhythmic in DD, we did not perform gene expression under these conditions, as the phase dispersion of the Cre+ mice at each timepoint would create too much noise and make data uninterpretable. We examined eight known circadian transcripts by qPCR, and all were identified as circadian via JTK_CYCLE analysis in Cre-;5xFAD mice under LD [27]. However, all showed blunted amplitude in Cre+;5xFAD mice under LD, with only *Nr1d1*/RevErbα remaining rhythmic, although phase advanced by 2 hours (Fig 2G, S2C). Thus, despite having partially-

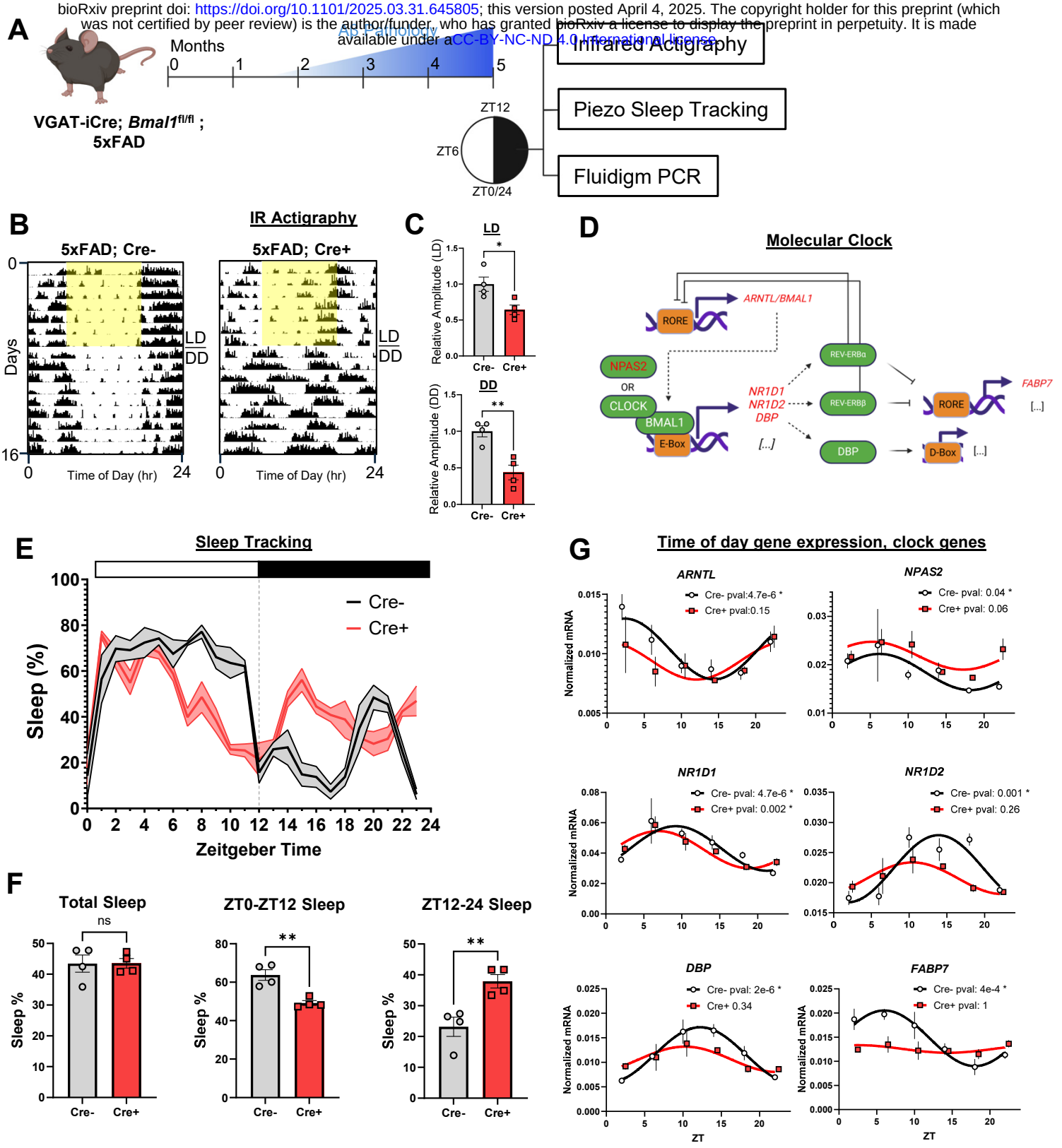

Figure 2. Loss of *Bmal1* in VGAT-expressing cells disrupts behavioral, sleep, and transcriptional rhythms in 5xFAD mice. A. Schematic of the experimental paradigm used to assess physiology in *VGAT-ires-Cre;Bmal$^{fl/fl}$;5xFAD* mice **B.** Representative actograms from *VGAT-ires-Cre;Bmal$^{fl/fl}$;5xFAD* mice. Mice were housed in 7 days of LD before being released into DD. **C.** Quantification of amplitude from B (n=4 mice per group as indicated, *p < 0.05 or ** p < 0.005 by Student's t) **D.** Diagram of the molecular clock, with measured genes highlighted in red **E.** Rolling hourly average sleep percentage in *VGAT-ires-Cre;Bmal$^{fl/fl}$;5xFAD* mice as a function of time. Black trace: Cre-negative 5xFAD controls. Red trace: Cre-positive 5xFAD mice. Zeitgeber time 0 (ZT0) defined as the start of the light period. **F.** Quantification of Total, ZT0-12 and ZT12-24 Sleep percentage. (**p < 0.005 by Student's t) **G.** Data points and cosinor fit of selected clock genes. Black circles are Cre-, Red squared are Cre+ (n=2-5 mice per genotype per time point. Benjamin-Hochberg adjusted p-values are displayed above each graph).

intact behavioral rhythms under LD conditions, circadian gene expression is disrupted in the hippocampus of Cre+ mice. Together, our data demonstrate that GABAergic *Bmal1* KO in 5xFAD mice disrupts both LD and DD circadian behavior, alters sleep distribution without changing total sleep amount, and dampens oscillatory hippocampal clock gene transcription. 0234

GABAergic *Bmal1* knockout reduces amyloid plaque pathology in light-dark

As circadian disruption is a hallmark of symptomatic Alzheimer's Disease, we next tested the hypothesis that excision of *Bmal1* in GABAergic neurons might influence Aβ aggregation in 5xFAD mice. We used exclusively female VGAT-Bmal1KO;5xFAD mice (Cre- and Cre+ littermates), as females have more aggressive plaque pathology, and kept mice under standard LD conditions until 5 months, when plaque accumulation is moderate. At 5 months staining with anti-Aβ antibody HJ3.4, which labels total Aβ plaque (diffuse and fibrillar), revealed a surprising reduction in plaque density within the cortex of roughly 40%, with smaller reductions of 25% in the hippocampal and thalamic regions (Fig 3A, 3B). As a partial explanation for these changes, we found a mild (~10%) but statistically significant reduction in plaque size within the cortex and hippocampus, along with a trending but non-significant reduction in plaque numbers in these regions (Fig 3D, 3E). Looking specifically at plaque numbers, histogram analysis revealed a significant reduction in the number of smaller plaques, between 30 and 250 square microns, in both the cortex and hippocampus (Fig 3F).

We next examined the accumulation of dense core fibrillar Aβ plaque using the congophilic stain X34. Despite no change in total X34 accumulation across regions, confocal imaging revealed changes in fibrillar plaque morphology typically indicative of lower toxicity: fibrillar plaques in the hippocampus in particular were more compact, with a smaller size and higher circularity index (Fig S3D). We co-stained sections with X34 and HJ3.4b, and found volumetric reductions of HJ3.4 around the volume of fibrillar plaques, as well as a reduction in the amount of diffuse, non-X34 associated HJ3.4, particularly within the hippocampus (Fig 3B, 3C). These data suggest that GABAergic *Bmal1* knockout alters the morphology of Aβ plaques and mitigates the aggregation of non-fibrillar plaque material.

GABAergic *Bmal1* knockout mitigates neuropil tau accumulation in light-dark

We next sought to look at how altered plaque aggregation at the regional level is accompanied by changes in the periplaque environment in Cre+ mice. Growth of amyloid plaques induces a combination of maladaptive responses in nearby neurites including axonal swelling, overexpression of Aβ-cleavage and lysosomal enzymes, and promotion of tau phosphorylation [28–30]. We stained for dystrophic neurites structurally via an antibody against the lysosomal enzyme LAMP1 and colocalized them around X34 plaques. We found no major change in the total volume of neuritic dystrophy nor in the amount of dystrophy per X34 plaque (Fig 4C, 4D) in any of the regions imaged. However, when we stained for neuropil (NP) phosphorylated (S202 & T205) tau using the antibody AT8 we found a dramatic reduction, with more than 75% of AT8 in the

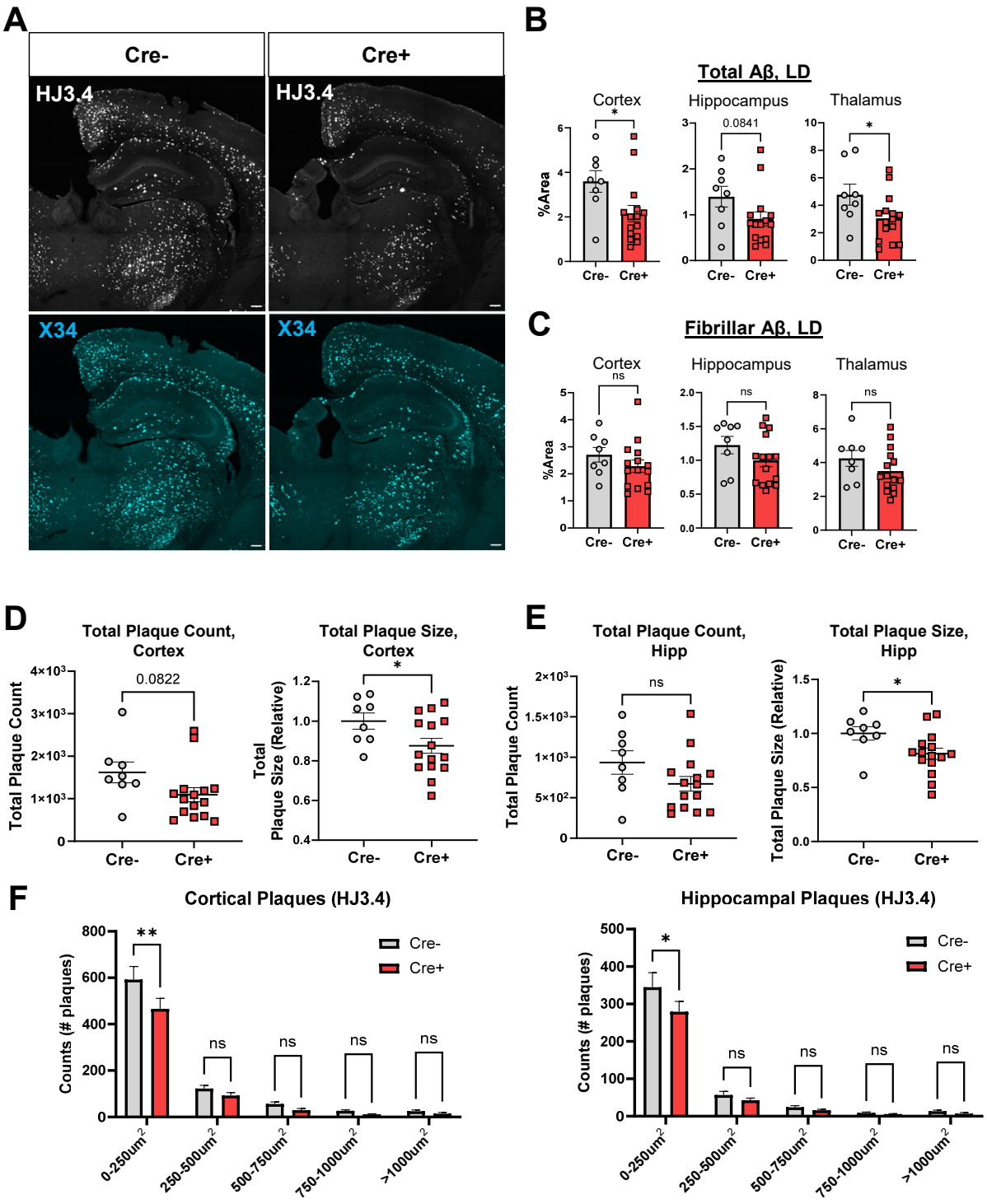

Figure 3. GABAergic BMAL1-knockout mitigates plaque accumulation under light-dark. A. Representative whole brain images from 5mo *VGAT-ires-Cre;Bmal$^{fl/fl}$;5xFAD* mice aged in light-dark, depicting staining by X34 (fibrillar plaques, cyan) and HJ3.4 (total plaques, white). (Scale bar = 200 μm) **B-C.** Quantification of plaque aggregation depicted in A. (n=9-15 mice per group as indicated. ns = not statistically significant, *p<0.05 by Students t, p-values between 0.05 and 0.1 are displayed) **D-E.** Quantification of cortical and hippocampal plaque total (HJ3.4) counts (first panel) and size (second panel) (n = 9-15 mice per group as indicated. *p < 0.05 by Students t, p-values between 0.05 and 0.1 are displayed) **F.** Histogram of total (HJ3.4) plaque counts in the cortex (left panel) and hippocampus (right panel) (n=9-15 mice per group, *p<0.05 or **p<0.05 by Two-Way ANOVA)

vicinity of imaged X34 plaques reduced per unit of X34 volume in both the hippocampus and thalamus (Fig 4A, 4B).

We also wanted to see if microglia, brain parenchymal immune cells who are capable of both protective and detrimental functions in the presence of Aβ pathology, may be implicated in the phenotypic changes seen in GABAergic BMAL1KO mice [31,32]. We used confocal imaging to characterize Iba1/CD68-double-positive microglia around X34+ plaques, which indicate phagocytic activated microglia. Though a trending decrease in Iba1+ volume around plaques in the cortex was noted, we saw no other major changes in any of our microglia markers between Cre- and Cre+ mice (Fig S4A, S4B). We also performed transcript analysis for various homeostatic and DAM (damage-associated microglia) markers on bulk hippocampal tissue and saw no statistical changes (Fig S4C) [33]. These data suggest GABAergic *Bmal1* knockout does not alter regional or periplaque microglial responses.

GABAergic *Bmal1* knockout has minimal effect on plaque pathology in constant darkness.

The effect of GABAergic *Bmal1* knockout on circadian behavior can be partially masked by the light-dark cycle, so we next asked if allowing Cre+ mice to be fully arrhythmic might modulate the effect on amyloid pathology. Starting at six weeks of age, we placed VGAT-BMAL1KO;5xFAD (Cre- and Cre+ littermates, all female) in constant darkness until age 5 months, when they were harvested and analyzed immunohistochemically for Aβ aggregation and related pathology as above. Surprisingly, Cre+;5xFAD mice kept in DD displayed no differences in total or fibrillar plaque density in any of the analyzed regions, as compared to Cre- controls (Fig 5A, 5B). At the peri-plaque level, no effect was seen on NP-tau aggregation using AT8. However, *Bmal1*-knockout mice did show consistent trend toward reductions in Lamp1-based neuritic dystrophy in all three regions, though none reached individual statistical significance (Fig 5D). Of note, we observed that mice kept in LD in our paradigm developed substantially more fibrillar plaques than those kept in DD, including a 70% increase in the cortex in both Cre- and Cre+ mice. This may suggest that VGAT-BMAL1KO acts to prevent plaque increases caused by LD exposure, thus only having an effect in the LD-exposed mice.

GABAergic *Bmal1* knockout alters APP processing in light-dark

We next sought to examine possible mechanisms of the effect of VGAT-BMAL1KO on plaque burden under LD conditions. As we did not see an effect on microglial markers, we next examined amyloid precursor protein (APP) processing. APP undergoes a series of proteolytic cleavages to be processed into Aβ. APP is first cleaved by beta secretase/BACE1 to form soluble APPβ (sAPPβ) and a β-carboxy terminal fragment (β-CTF). sAPPβ is then further cleaved by the gamma secretase complex – which includes AD risk gene products PSEN1 and PSEN2, to produce Aβ [34,35]. Alternatively, APP can be processed first by alpha secretases to produce non-amyloidogenic products, including α-carboxy terminal fragment (α-CTF). As a proxy for APP processing, we first measured the levels of mouse *BACE1* and *PSEN1* transcripts in bulk hippocampus at six time points. Stratifying by time-of-day, we found a statistically significant rhythm in *mPSEN1* transcript in Cre- mice that was lost in GABAergic *Bmal1* knockout. The overall expression of PSEN1 was also suppressed, albeit mildly (20%). Similar

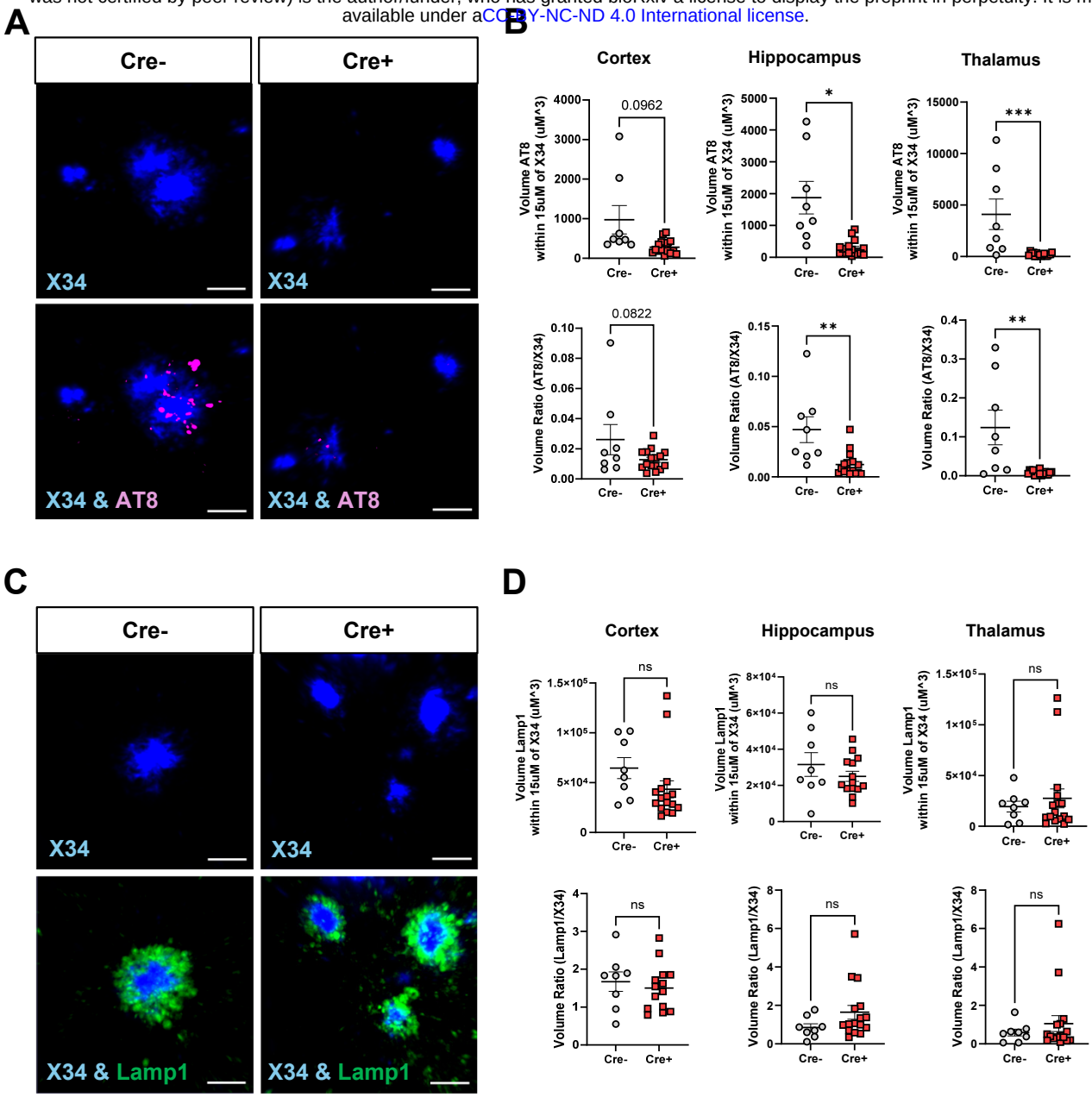

Figure 4. GABAergic BMAL1-knockout mitigates neuropil tau aggregation under light-dark. A. Representative confocal images depicting fibrillar plaque (blue, X34) and phospho-tau (magenta, AT8) (Scale bar, 20 μm) **B.** Quantification from (A) Top: averaged total AT8 volume per field. Bottom: total AT8 volume per field divided by X34 volume. (n = 9-15 mice per group, *p < 0.05 or **p<0.005 or ***p<0.0005 by Students t, p-values between 0.05 and 0.1 are displayed) **C.** Representative confocal images depicting fibrillar plaque (blue, X34) and neuritic dystrophy (green, Lamp1) (Scale bar, 20 μm) **D.** Quantification from (A) Top: averaged total Lamp1 volume per field. Bottom: total Lamp1 volume per field divided by X34 volume. (n = 9-15 mice per group, ns=not statistically significant)

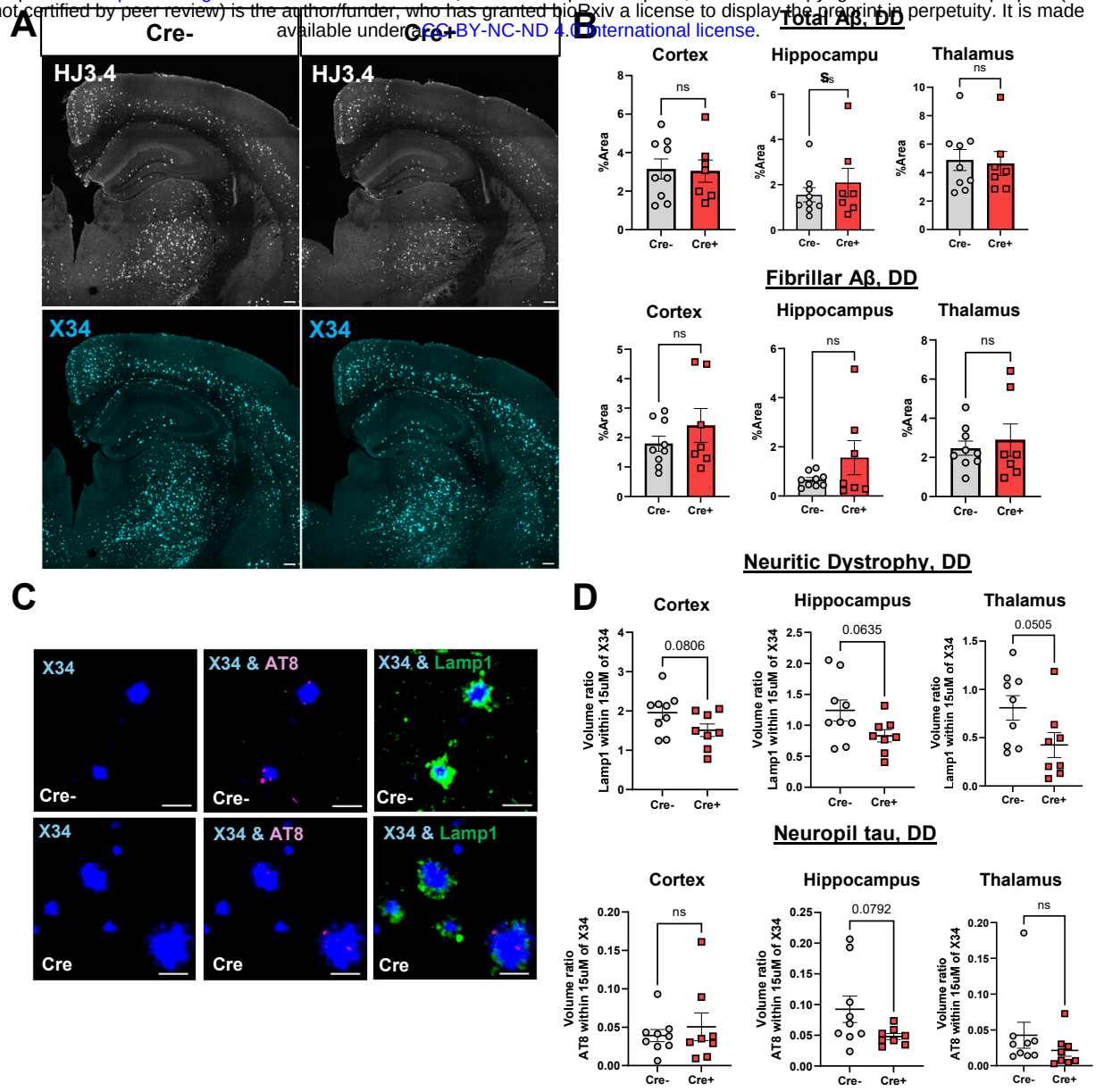

Figure 5. **GABAergic BMAL1-knockout has minimal impact on regional and periplaque pathology under constant darkness**. **A.** Representative whole brain images from 5mo *VGAT-ires-Cre;Bmal*$^{fl/fl}$*;5xFAD* mice aged in constant darkness, depicting staining by X34 (fibrillar plaques, cyan) and HJ3.4 (total plaques, white). (Scale bar = 200 μm) **B.** Quantification of total (top) and fibrillar (bottom) plaque aggregation from labelled regions as depicted in A. (n=7-9 mice per group as indicated. ns = not statistically significant) **C.** Representative confocal images depicting fibrillar plaque (blue, X34), phospho-tau (magenta, AT8), and neuritic dystrophy (green, Lamp1) (Scale bar, 20 μm) **D.** Quantification from (C) Top: averaged total Lamp1 volume divided by X34 volume per field. Bottom: averaged total AT8 volume divided by X34 volume. (n = 7-9 mice per group, ns= not statistically significant, p-values between 0.05 and 0.1 are displayed

examination of *BACE1* transcript revealed no rhythmic activity, nor any statistically significant change in overall expression (Fig 6A). Expression of both transcripts in DD mice was unchanged in Cre+ mice relative to Cre-, suggesting that suppression of mouse PSEN1 transcript by *Bmal1*-knockout may be light-dependent. We next analyzed the levels of APP processing proteins and products via immunoblotting cortical lysates from LD treated mice. Total CTF amount (α-CTF + β-CTF) relative to full-length (FL) APP was decreased in Cre+ mice relative to Cre- littermates, suggesting that proteolytic conversion of APP via amyloidogenic and non-amyloidogenic pathways may be suppressed in VGAT-BMAL1 KO mice. However, levels of BACE1 and PSEN1 protein remained similar in Cre+ and Cre- mice (Fig 6B, 6C). With regard to PSEN1, this may be partially explained by the PSEN1 antibody measuring both endogenous murine and transgenic human PSEN1 from the 5xFAD transgene, the latter of which may be unaffected GABAergic *Bmal1*-knockout. These data suggest that GABAergic *Bmal1* knockout in LD suppresses APP proteolytic processing, possibly by inhibiting expression of murine presenilin 1 transcript.

Discussion

Disruption of circadian rhythms is highly prevalent in neurological disorders such as Alzheimer's Disease. Age, the primary risk factor for developing AD, may contribute to disease progression partly through age-related circadian decline [36]. Aβ pathology starts to develop roughly 20 years before the development of cognitive symptoms. In the vast majority of AD patients this constitutes middle age, the same epoch in which the strength of transcriptional and hormonal circadian rhythms begins to decline [37–39]. Thus, we wanted to examine whether circadian fragmentation could influence Aβ related pathology, including plaque-induced neuritic dystrophy, and NP tau aggregation. Given the SCN's principal role in regulating circadian rhythms, we employed a genetic model of SCN disruption using VGAT-iCre with high expression within the SCN to drive *Bmal1* deletion; GABAergic *Bmal1*-knockout mice demonstrated behavioral circadian deficits in both LD and DD, as well as deconsolidated sleep and clock gene rhythms within the hippocampus. When crossed to 5xFAD mice, VGAT-BMAL1KO unexpectedly mitigated amyloid plaque accumulation and plaque-associated tau phosphorylation, as well as reduced mPSEN1 expression and amyloidogenic APP cleavage. However, this only occurred when mice were kept under standard LD conditions, and not when mice were fully arrhythmic and removed from all light cues under DD conditions. Moreover, 5xFAD mice kept under DD had less plaque burden in general. Our data suggest that the central circadian clock interacts with the light-dark cycle to regulate amyloid plaque accumulation and tau phosphorylation in a complex manner which was not previously appreciated.

Previous studies have shown that interstitial fluid Aβ has a strong diurnal rhythm under basal light-dark conditions in mice which is directly related to rhythms in neuronal activity [12,40,41]. However, the role of the circadian clock in regulating APP processing directly is unknown. While we have not examined circadian regulation of APP metabolism directly, our experiments show that GABAergic *Bmal1* KO suppresses APP cleavage to produce CTFs, suggesting reduced Aβ production. This finding is

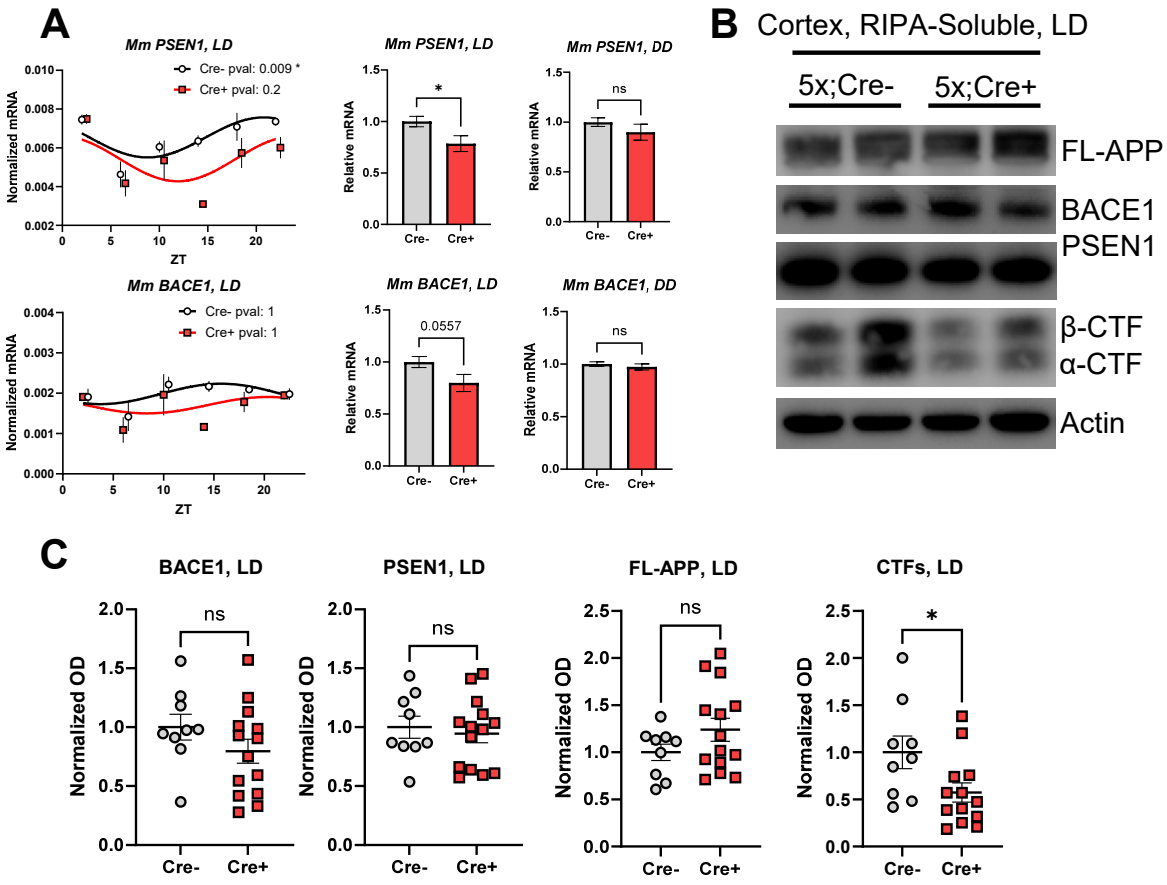

Figure 6. **GABAergic BMAL1-knockout alters APP processing in light-dark. A.** (Left) Data points and cosinor fit of murine *BACE1* and *PSEN1* transcripts over time. Black circles are Cre-, Red squared are Cre+ (n=2-5 mice per genotype per time point. Benjamin-Hochberg adjusted p-values are displayed above each graph). (Right) Bulk expression of transcripts collapse across time points. (n=9-15 mice per genotype per group in LD, and 6 mice per group in DD. ns=not statistically significant, * p<0.05 by Students t, p-values between 0.05 and 0.1 are displayed) **B.** Immunoblot assessing expression of APP processing enzymes, full-length amyloid, and C-terminal fractions in soluble brain lysates from cortical brain tissue. **C.** Quantification of B (n = 9-15 mice per group as indicated, ns = not statistically significant, * p < 0.05 as indicated.

associated with loss of the normal diurnal expression rhythm of murine *PSEN1* under LD, culminating in overall decreased mPSEN1 expression. While the pool of total (human + mouse) PSEN1 protein appears to be unaffected, inhibition of the murine copy may partially explain the reduction of CTF peptides relative to full-length APP under light-dark, given that mouse PSEN1 is capable of cleaving human sAPPβ into plaque-generating Aβ [42]. While these data provide a partial explanation of reduced plaque load in *Bmal1* knockout mice, further studies will be necessary to examine how both light exposure and the circadian clock regulate APP metabolism at the genetic and functional levels.

The analysis of plaque development in both light-dark and constant darkness allowed us to evaluate the effects of GABAergic *Bmal1* knockout on Aβ pathology in both masking (LD) and non-masking (DD) environments [43]. With respect to both circadian amplitude and period, *Bmal1* knockout mice in constant darkness exhibited a more severe circadian disruption than *Bmal1* knockout in light-dark, relative to Cre- littermates. We expected that masking might mitigate plaque accumulation, as compared to full arrhythmicity in DD. However, Cre+ mice in LD had reduced amyloid pathology as compared to Cre- in LD, while Cre+ and Cre- mice in DD exhibited no differences in regional plaque pathology, and only non-significant reductions in neuritic dystrophy at the peri-plaque level. One possible reason for the change in plaques in light-dark but not constant darkness treated mice may be that *Bmal1* knockout in LD shifts circadian behavior with respect to the light cycle, causing mild desynchrony between the activity rhythm and the light cycle, as evidence by an earlier activity onset time and *Nr1d1* gene expression. Such a desynchrony is not possible in constant darkness, and may have underlying effects on Aβ pathology that are not recapitulated by arrythmicity [44]. Future studies can directly test this hypothesis by comparing plaque development in mice exposed to phase-delaying light schedules to those left in standard LD [45]. From a general mechanistic standpoint, it remains unclear how VGAT-KO reduces amyloid pathology only under LD conditions. One speculative explanation for our findings is that under LD conditions in mice with a competent central clock, that the light-dark cycle and circadian rhythm reinforce one another to produce larger amplitude rhythms in activity and Aβ production in the brain, leading to more amyloid production. If one of these factors, either the central clock (as in VGAT-BMAL1KO mice) or the light-dark cycle (as in DD), are removed, this synergy is disrupted and there is less plaque formation. While this hypothesis would need to be confirmed in other amyloid models and paradigms, it could change our thinking about the relationship between light cycles, circadian rhythms, and amyloid. One piece of evidence against this hypothesis comes from a previous study by Nagare et al. which demonstrated that stronger light-dark lighting cycles (achieved with brighter lighting during the light phase) reduced cortical Aβ42 levels in 11mo 5xFAD mice [46]. This outcome would not be predicted based on our hypothesis and data herein. However, it is difficult to compare the Nagare study with ours, as Nagare et al used much older mice (with more established/severe plaque burden), did not examine amyloid plaque pathology (only Aβ ELISA), and did not directly manipulate the circadian clock. Regardless of the exact mechanism, together these sets of experiments suggest a revision of the proposed simple positive feedback loop between circadian rhythm disruption and Aβ pathology, and suggest that APP

processing may be vulnerable to therapeutic intervention in a light- and clock-dependent manner.

Our finding that VGAT-BMAL1KO;5xFAD mice accumulate less plaque under LD conditions is perhaps unexpected, based on our published findings and the general idea that circadian disruption should be detrimental in AD. Previous work from our lab showed that post-natal whole-body *Bmal1* deletion accelerated plaque accumulation in APP/PS1-21 mice, which harbor different APP and PS1 mutations than 5xFAD and tend to accumulate mostly fibrillar plaques [47]. Thus, that study differs from this one both in terms of the amyloid model, as well as the type of *Bmal1* deletion (global post-natal deletion vs. germline deletion in GABAergic neurons). BMAL1 exerts many effects on non-neuronal cell types in the brain, and throughout the periphery, which could impact plaque formation in global KOs, while VGAT-mediated deletion should not have these effects [48]. Future studies in which we generate mice the VGAT-BMAL1KO on the APP/PS1-21 background could help determine if these discrepancies in phenotype are due to differences between the APP/PS1-21 and 5xFAD models, which might indicate that the circadian system influences different amyloid deposition differently based on the specific attributes of the model (such as the Aβ40/42 ratios, specific mutation effect, type and distribution of plaques, and rate/age of accumulation). It also remains possible that VGAT-BMAL1KO alters inhibitory tone in the brain, leading to changes in activity-related Aβ production and aggregation (independent of effects on circadian rhythms) [40,49,50]. However, in that case, we would expect to see similar effects of VGAT-BMAL1KO in both LD and DD conditions, which was not the case. However, replicating our findings using a more SCN-specific Cre, or another neuron-specific Cre, to delete *Bmal1* (in non-GABAergic neurons) could be a next step. Moreover, moving into more naturalistic models of circadian disruption, such as “jet lag” models which induce circadian desynchrony via shifting of the light-dark cycle, is an important next step in order to increase the generalizability of findings to humans.

A notable finding from our study is the reduction in peri-plaque tau phosphorylation in VGAT-BMAL1KO;5xFAD mice in LD. This was independent of the effect on overall plaque burden, as it persisted analyzed on a per-plaque basis. This result may suggest a decrease in the toxicity of plaques in *Bmal1* knockout mice in LD which could reflect a change in plaque composition. While we are unaware of any previous studies examining the effects of circadian manipulation on plaque-related tau phosphorylation, it is notable that our group has previously shown the global or astrocyte-specific *Bmal1* KO can mitigate tau pathology in the P301S PS19 tauopathy model [51]. In that work, the anti-tau effect was attributed to changes in astrocyte proteostatic function, though the mechanism is likely different in this model, as astrocyte *Bmal1* is intact in VGAT-BMAL1KO;5xFAD mice. Future studies could use plaque-associated tau seeding models to examine the impact of circadian disruption on amyloid-tau interactions.

In summary, we have found that deletion of *Bmal1* specifically in VGAT-expressing GABAergic neurons, which fully disrupts central circadian clock function, unexpectedly reduces amyloid plaque burden and tau phosphorylation in 5xFAD, and that this effect is eliminated when mice are maintained in constant darkness. Our findings suggest complex interaction between circadian rhythms and the light-dark cycle in regulating

amyloid pathology and provide new insights into how circadian function might be optimized or manipulated to prevent AD.

Materials and Methods

Mice

All animal procedures were approved by the Washington University IACUC and were conducted in agreement with AALAC guidelines and under supervision of the Washington University Department of Comparative Medicine. 5xFAD mice were generated from mice originally purchased through The Jackson Laboratory (MMRRC; stock no. 34848). VGAT-ires-iCre C57Bl6j (Jackson Laboratory 028862) were a generous donation from David R. Weaver. VGAT-ires-iCre mice were bred at least 3 generations to generate appropriate Cre and floxed alleles, and Cre+ and Cre- littermates were compared to one another. Both male and female mice were used.

For aging 5xFAD mice in constant darkness and light-dark, mice were transferred into custom-built tents with ventilation and light manipulation. Mice were group housed, and food and water provided *ad-libitum*. We exposed mice to either a 12h:12h light/dark (LD, where lights on is defined as zeitgeber time ZT0) or 12h:12h dark/dark (DD) with temperature range 20-26 °C and 50-60% humidity. A visual inspection was performed once a week during cage changes. Unless otherwise specified, all mice were perfused and tissues harvested at 5 months of age.

Circadian Activity Measurement

Mice were transferred into single cages in custom-built tents for no more than four weeks during recordings, and food and water provided *ad-libitum*. Mice were acclimatized for one week in LD before data acquisition. Activity was recorded via motion-tracking infrared wireless nodes (Actimetrics), one per cage. Circadian statistical measures were plotted and analyzed via Clocklab 6.1.02 and Graphpad Prism 10.4.1. Free-running period was calculated by X^2 periodogram using 8 days before the transition from LD to DD, and 8 days starting two days after the LD to DD transition. Fast Fourier Transform (FFT) was used to calculate the relative amplitude of the circadian component from 18 to 30hr. Animals with a loss of circadian rhythms were excluded from period calculations.

Sleep Measurement

Sleep measurement was performed using the PiezoSleep mouse behavioral tracking system (Signal Solutions, LLC, Lexington, KY, USA) [52]. This method utilized a thin dielectric piezo sensors that generates a signal in response to pressure changes on its surface. Mice were individually housed in home cages with the piezo pad underneath, and were acclimated to housing conditions for one week before the start of data

collection. They were given fresh bedding as well as food and water *ad libitum*. Cre- and Cre+ littermates, either 5xFAD- or 5xFAD+ were continuously monitored over the course of two weeks (7x LD, 7x DD). Data was acquired and analyzed using SleepStats software (Signal Solutions, LLC, Lexington, KY, USA).

Immunohistochemistry

Mice were anesthetized with 150mg/kg ip pentobarbital and perfused for 3 minutes with cold Dulbecco's modified PBS with 3% heparin. One hemisphere was dissected into cortical and hippocampal regions, flash frozen, and stored at -80 for RNA and biochemical analysis. The other was fixed in 4% PFA for 24 hours at 4°C. Brains were sectioned on a sliding microtome in 40-micron sections and stored in cryoprotectant (30% ethylene glycol, 15% sucrose 15% phosphate buffer in ddH2O). For fibrillar plaque saining, sections were washed in TBS, incubated in TBS+0.25% Triton X-100 for 30 min, then incubated in X34 staining buffer (10uM X34 and 20mM NaOH in 60% PBS, 40% ethanol) for 20 min. Sections were then blocked in 3% donkey serum for one hour, then incubated in TBSX containing 1% donkey serum and primary antibodies overnight at 4° C. The following primary antibodies were used: Rat anti-Lamp1 (DSHB, 1D4B), biotinylated AT8 (Thermo, MN1020B), goat anti-Iba1 (Abcam, ab5076), rat anti-CD68 (BioRad, MCA1957). Biotinylated HJ3.4 was generously provided by David M. Holtzman. On day 2, sections were washed and incubated in 1:1000 donkey fluorescent secondary antibodies before being mounted on slides using Prolong Gold.

Image Acquisition and analysis

Images were obtained from 2 sections per mouse, 200 microns apart. Slides were scanned on a W1 CSU SoRa Spinning Disk Confocal (Nikon) and processed using ImageJ version 1.54 (National Institutes of Health). For whole region analysis, a stitched image was generated from a 3x by 3x tiling of 9x z-stacks (40 micron) of each section using the 10x objective generating a final image at 6682 by 6682 pixel resolution, then processed via a maximum intensity projection. Laser and detector settings were set for the acquisition of each image consistently. Peri-plaque images were acquired with a 20x objective, 2x zoom at 1,024 x 1,024 resolution.

Peri-plaque images were analyzed on a semi-automated platorm using Imaris 9.5 (Bitplane) and MATLAB. Surfaces were created using X34, dilated by 15 microns, and colocalized with various immunostained surfaces. For volume ratio calculations, the combined volume of each given surface in an image was divided by the combined X-34. All staining experiments were imaged and quantified by a blinded investigator.

RNA Quantification and Analysis

Tissue was homogenized in 500uL of Trizol with RNAse free beads in a bullet blender for 4 minutes. Trizol samples were then extracted with 1:6 chloroform and centrifugation at 12,500g for 15 minutes. RNA was extracted from the aqueous layer using PureLink

RNA Mini Kit according to the manufacturer's protocol. Nanodrop spectrophotometry was used to determine the RNA concentration, after which the samples were converted into cDNA using a high capacity RNA-cDNA reverse transcriptase kit (Applied Biosystems) with 400-800 g RNA per 20 uL reaction. We performed qPCR using ABI Taqman Primers and ABI PCR Master Mix Buffer on ABI StepOnePLus or QuantStudio 12K thermocyclers. Taqman primers (Invitrogen) were used, and mRNA values were normalized to β-Actin (Actb) or Gapdh. For microfluidic experiments, qPCR array measurements were performed by the Washington University Genome Technology Access Center (GTAC) using a Fluidigm Biomark HD system, again using Taqman primers and normalized to GAPDH.

Protein Extraction

Flash frozen hippocampal brain tissue was immersed in RIPA buffer pH 8.0: 150mM NaCl, 50mM Tris, 0.5% deoxycholic acid, 1% Triton X-100, 0.1% SDS, 5mM EDTA, 20mM NaF, and 1mM sodium orthovanadate supplemented with 1% protease and phosphatase inhibitor. Tissue was ground on ice for 15 seconds using a tissue homogenizer and centrifuged at 4°C at 10,000g for 5 minutes. The resulting supernatant was taken as the soluble fraction. The pellet was incubated in 1:6 5M guanidine hydrochloride, subjected to ultrasonication for 30 seconds, and incubated at room temperature for 2 hours with shaking. The resulting homogenate was then centrifuged for at 4°C at 20,000g for 20 minutes, and the supernatant collected as the insoluble fraction for long-term storage at -80. Protein concentration was analyze via Pierce BCA Protein Assay (Thermo).

Western Blot

Hippocampal and cortical samples were weighed and lysed according to the protein extraction protocol specified above. Equal amounts of protein samples (10-20ug) were dissolved in sample buffer, heat treated at 95° C for 5 minutes, and treated to sodium dodecyl sulfate-polyacrylamide get electrophoresis before electrophoretic transfer to immunoblotting 0.2um PVDF membranes. The membranes were then pretreated with a blocking solution (8% dry skim milk in TBS, 0.1% Tween 20) for 1h at room temperature, then treated with primary antibodies overnight at 4° C. The following primary antibodies were used: Rabbit anti-β amyloid (Thermo, #51-2700, 1:1000), Rabbit anti-PSEN1 (CST #5643, 1:1000), Rabbit anti-BACE1 (Abcam, EPR3956, 1:1000), Rabbit anti-β actin (CST #4970. The next day, after three washes with TBST, membranes were incubated in horseradish peroxidase (HRP)-conjugated secondary antibodies against rabbit IgG in 1% BSA for 1 hour at room temperature. Proteins were detected by chemiluminescence using Super Signal Wes Pico PLUS Chemiluminescent Substrate (Thermo, #34577). Western blots were visualized using a ChemiDoc Imaging System (BioRad) and analyzed with ImageJ. Unless otherwise specified, blots were normalized to Actin.

Statistics

Graphs display the mean+/- SEM, and n indicates the number of animals, unless otherwise indicated in the figure legend. To examine if variances were different, an F test was first performed for datasets with a single dependent variable and two groups. If not, a two-tailed unpaired t0test was performed. If variances were significantly different, a non-parametric Mann-Whitney U test was performed. For datasets with two dependent variables, 2-way ANOVA was performed. And if the main effect was significant, Sidak multiple comparisons test was applied for the variables. Outliers were identified using ROUT (Q = 1%) and excluded. Statistical tests were performed with GraphPad Prizm software version 10.4.1. P values greater than 0.1 were not as not significant (NS), while P values from 0.1-005 were specifically listed in the figure. P < 0.05 was considered significant and notes with asterisks indicating the p-value: *P < 0.05, ** < 0.005, *** < 0.0005

Acknowledgements

This work was financed by grant R01AG05451707 (ESM) from the National Institutes of Health, as well as a Personal Medicine Initiative award from Washington University. High-Throughput PCR was performed by the GTAC at the McDonnell Genome Institute at Washington University. AS was funded in part by the BrightFocus Foundation grant number A2024031F. The GTAC is partially supported by NCI Cancer Center Support grant P30 CA91842 to Siteman Cancer Center, ICTS.CTSA grant UL1TR002345 from the National Center for Research Resources (NCRR), a component of the NIH, and NIH Roadmap for Medical Research. We thank the Washington University Center for Cellular Imaging (WUCCI) for assistance with confocal microscopy. WUCCI is supported by Washington University School of Medicine, The Children's Discovery Institute of Washington University and St. Louis Children's Hospital (CDI-CORE-2015-505 and CDI-CORE-2019-813), and the Foundation for Barnes-Jewish Hospital (nos. 3770 and 4642).

References

1. 2024 Alzheimer's disease facts and figures (2024). Alzheimer's Dement. *20*, 3708–3821. https://doi.org/10.1002/alz.13809.

2. Khachiyants N, Trinkle D, Son SJ, Kim KY (2011). Sundown syndrome in persons with dementia: An update. Psychiatry Investig. *8*, 275–287.

3. Hatfield, C.F., Herbert, J., Van Someren, E.J.W., Hodges, J.R., and Hastings, M.H. (2004). Disrupted daily activity/rest cycles in relation to daily cortisol rhythms

of home-dwelling patients with early Alzheimer's dementia. Brain *127*, 1061–1074. https://doi.org/10.1093/brain/awh129.

4. Musiek, E.S., and Holtzman, D.M. (2016). Mechanisms linking circadian clocks, sleep, and neurodegeneration. Science (80-.). *354*, 1004–1008. https://doi.org/10.1126/science.aah4968.

5. Czeisler, C.A., Dumont, M., Duffy, J.F., Steinberg, J.D., Richardson, G.S., Brown, E.N., Sánchez, R., Ríos, C.D., and Ronda, J.M. (1992). Association of sleep-wake habits in older people with changes in output of circadian pacemaker. Lancet *340*, 933–936. https://doi.org/10.1016/0140-6736(92)92817-Y.

6. Talamanca, L., Gobet, C., and Naef, F. (2023). Sex-dimorphic and age-dependent organization of 24-hour gene expression rhythms in humans. Science (80-.). *379*, 478–483. https://doi.org/10.1126/science.add0846.

7. Musiek, E.S., Bhimasani, M., Zangrilli, M.A., Morris, J.C., Holtzman, D.M., and Ju, Y.E.S. (2018). Circadian rest-activity pattern changes in aging and preclinical Alzheimer disease. JAMA Neurol. *75*, 582–590. https://doi.org/10.1001/jamaneurol.2017.4719.

8. Musiek, E.S., Lim, M.M., Yang, G., Bauer, A.Q., Qi, L., Lee, Y., Roh, J.H., Ortiz-Gonzalez, X., Dearborn, J.T., Culver, J.P., et al. (2013). Circadian clock proteins regulate neuronal redox homeostasis and neurodegeneration. J. Clin. Invest. *123*, 5389–5400. https://doi.org/10.1172/JCI70317.

9. Lananna, B. V., Nadarajah, C.J., Izumo, M., Cedeño, M.R., Xiong, D.D., Dimitry, J., Tso, C.F., McKee, C.A., Griffin, P., Sheehan, P.W., et al. (2018). Cell-Autonomous Regulation of Astrocyte Activation by the Circadian Clock Protein BMAL1. Cell Rep. *25*, 1-9.e5. https://doi.org/10.1016/j.celrep.2018.09.015.

10. Radcliffe, L.A., Bradfield, C.A., Clendenin, C., Simon, M.C., Moran, S.M., Hogenesch, J.B., Takahashi, J.S., Wilsbacher, L.D., and Bunger, M.K. (2000). Mop3 is an essential component of the master circadian pacemaker in mammals. Cell *103*, 1009–1017.

11. Yang, G., Chen, L., Grant, G.R., Paschos, G., Song, W.L., Musiek, E.S., Lee, V., McLoughlin, S.C., Grosser, T., Cotsarelis, G., et al. (2016). Timing of expression of the core clock gene Bmal1 influences its effects on aging and survival. Sci. Transl. Med. *8*. https://doi.org/10.1126/scitranslmed.aad3305.

12. Kress, G.J., Liao, F., Dimitry, J., Cedeno, M.R., FitzGerald, G.A., Holtzman, D.M., Musiek, E.S. (2018). Regulation of amyloid-β dynamics and pathology by the circadian clock. J. Exp. Med. *215*, 1059–1068.

13. Zhou JN, Hofman MA, Swaab DF. (1995). VIP neurons in the human SCN in relation to sex, age, and Alzheimer's disease. Neurobiol. Aging *16*, 571–576.

14. Damiola, F., Le Minh, N., Preitner, N., Kornmann, B., Fleury-Olela, F., and Schibler, U. (2000). Restricted feeding uncouples circadian oscillators in peripheral tissues from the central pacemaker in the suprachiasmatic nucleus.

Genes Dev. *14*, 2950–2961.

15. Weaver, D.R., van der Vinne, V., Giannaris, E.L., Vajtay, T.J., Holloway, K.L., and Anaclet, C. (2018). Functionally Complete Excision of Conditional Alleles in the Mouse Suprachiasmatic Nucleus by Vgat-ires-Cre. J. Biol. Rhythms *33*, 179–191. https://doi.org/10.1177/0748730418757006.

16. Vong, L., Ye, C., Yang, Z., Choi, B., Chua, S., and Lowell, B.B. (2011). Leptin Action on GABAergic Neurons Prevents Obesity and Reduces Inhibitory Tone to POMC Neurons. Neuron *71*, 142–154. https://doi.org/10.1016/j.neuron.2011.05.028.

17. Lee, I.T., Chang, A.S., Manandhar, M., Shan, Y., Fan, J., Izumo, M., Ikeda, Y., Motoike, T., Dixon, S., Seinfeld, J.E., et al. (2015). Neuromedin s-producing neurons act as essential pacemakers in the suprachiasmatic nucleus to couple clock neurons and dictate circadian rhythms. Neuron *85*, 1086–1102. https://doi.org/10.1016/j.neuron.2015.02.006.

18. Husse, J., Leliavski, A., Tsang, A.H., Oster, H., and Eichele, G. (2014). The light-dark cycle controls peripheral rhythmicity in mice with a genetically ablated suprachiasmatic nucleus clock. FASEB J. *28*, 4950–4960. https://doi.org/10.1096/fj.14-256594.

19. Oakley, H., Cole, S.L., Logan, S., Maus, E., Shao, P., Craft, J., Guillozet-Bongaarts, A., Ohno, M., Disterhoft, J., Van Eldik, L., et al. (2006). Intraneuronal β-amyloid aggregates, neurodegeneration, and neuron loss in transgenic mice with five familial Alzheimer's disease mutations: Potential factors in amyloid plaque formation. J. Neurosci. *26*, 10129–10140. https://doi.org/10.1523/JNEUROSCI.1202-06.2006.

20. Madisen, L., Zwingman, T.A., Sunkin, S.M., Oh, S.W., Zariwala, H.A., Gu, H., Ng, L.L., Palmiter, R.D., Hawrylycz, M.J., Jones, A.R., et al. (2010). A robust and high-throughput Cre reporting and characterization system for the whole mouse brain. Nat. Neurosci. *13*, 133–140. https://doi.org/10.1038/nn.2467.

21. Chaudhry, F.A., Reimer, R.J., Bellocchio, E.E., Danbolt, N.C., Osen, K.K., Edwards, R.H., and Storm-Mathisen, J. (1998). The vesicular GABA transporter, VGAT, localizes to synaptic vesicles in sets of glycinergic as well as GABAergic neurons. J. Neurosci. *18*, 9733–9750. https://doi.org/10.1523/jneurosci.18-23-09733.1998.

22. Himali, J.J., Baril, A.A., Cavuoto, M.G., Yiallourou, S., Wiedner, C.D., Himali, D., Decarli, C., Redline, S., Beiser, A.S., Seshadri, S., et al. (2023). Association between Slow-Wave Sleep Loss and Incident Dementia. JAMA Neurol. *80*, 1326–1333. https://doi.org/10.1001/jamaneurol.2023.3889.

23. Winer, J.R., Deters, K.D., Kennedy, G., Jin, M., Goldstein-Piekarski, A., Poston, K.L., and Mormino, E.C. (2021). Association of Short and Long Sleep Duration with Amyloid-ß Burden and Cognition in Aging. JAMA Neurol. *78*, 1187–1196. https://doi.org/10.1001/jamaneurol.2021.2876.

24. Wang, C., Nambiar, A., Strickland, M.R., Lee, C., Parhizkar, S., Moore, A.C., Musiek, E.S., Ulrich, J.D., and Holtzman, D.M. (2023). APOE-ε4 synergizes with sleep disruption to accelerate Aβ deposition and Aβ-associated tau seeding and spreading. J. Clin. Invest. *133*. https://doi.org/10.1172/JCI169131.

25. Kang, J.E., Lim, M.M., Bateman, R.J., Lee, J.J., Smyth, L.P., Cirrito, J.R., Fujiki, N., Nishino, S., and Holtzman, D.M. (2009). Amyloid-β dynamics are regulated by orexin and the sleep-wake cycle. Science (80-.). *326*, 1005–1007. https://doi.org/10.1126/science.1180962.

26. Parhizkar, S., Gent, G., Chen, Y., Rensing, N., Gratuze, M., Strout, G., Sviben, S., Tycksen, E., Zhang, Q., Gilmore, P.E., et al. (2023). Sleep deprivation exacerbates microglial reactivity and Aβ deposition in a TREM2-dependent manner in mice. Sci. Transl. Med. *15*. https://doi.org/10.1126/scitranslmed.ade6285.

27. Hughes, M.E., Hogenesch, J.B., and Kornacker, K. (2010). JTK-CYCLE: An efficient nonparametric algorithm for detecting rhythmic components in genome-scale data sets. J. Biol. Rhythms *25*, 372–380. https://doi.org/10.1177/0748730410379711.

28. Gowrishankar, S., Yuan, P., Wu, Y., Schrag, M., Paradise, S., Grutzendler, J., De Camilli, P., and Ferguson, S.M. (2015). Massive accumulation of luminal protease-deficient axonal lysosomes at Alzheimer's disease amyloid plaques. Proc. Natl. Acad. Sci. U. S. A. *112*, E3699–E3708. https://doi.org/10.1073/pnas.1510329112.

29. He, Z., Guo, J.L., McBride, J.D., Narasimhan, S., Kim, H., Changolkar, L., Zhang, B., Gathagan, R.J., Yue, C., Dengler, C., et al. (2018). Amyloid-β plaques enhance Alzheimer's brain tau-seeded pathologies by facilitating neuritic plaque tau aggregation. Nat. Med. *24*, 29–38. https://doi.org/10.1038/nm.4443.

30. Sadleir, K.R., Kandalepas, P.C., Buggia-Prévot, V., Nicholson, D.A., Thinakaran, G., and Vassar, R. (2016). Presynaptic dystrophic neurites surrounding amyloid plaques are sites of microtubule disruption, BACE1 elevation, and increased Aβ generation in Alzheimer's disease. Acta Neuropathol. *132*, 235–256. https://doi.org/10.1007/s00401-016-1558-9.

31. Sosna, J., Philipp, S., Albay, R.I., Reyes-Ruiz, J.M., Baglietto-Vargas, D., LaFerla, F.M., and Glabe, C.G. (2018). Early long-term administration of the CSF1R inhibitor PLX3397 ablates microglia and reduces accumulation of intraneuronal amyloid, neuritic plaque deposition and pre-fibrillar oligomers in 5XFAD mouse model of Alzheimer's disease. Mol. Neurodegener. *13*. https://doi.org/10.1186/s13024-018-0244-x.

32. Kiani Shabestari, S., Morabito, S., Danhash, E.P., McQuade, A., Sanchez, J.R., Miyoshi, E., Chadarevian, J.P., Claes, C., Coburn, M.A., Hasselmann, J., et al. (2022). Absence of microglia promotes diverse pathologies and early lethality in Alzheimer's disease mice. Cell Rep. *39*. https://doi.org/10.1016/j.celrep.2022.110961.

33. Keren-Shaul, H., Spinrad, A., Weiner, A., Matcovitch-Natan, O., Dvir-Szternfeld, R., Ulland, T.K., David, E., Baruch, K., Lara-Astaiso, D., Toth, B., et al. (2017). A Unique Microglia Type Associated with Restricting Development of Alzheimer's Disease. Cell *169*, 1276-1290.e17. https://doi.org/10.1016/j.cell.2017.05.018.

34. Sherrington, R., Leresque, G., Ikeda, M., Ch, H., Lin, C., Holman, K., Tsuda, T., Mar, L., Foncin, J., Bruni, A.C., et al. (1995). Cloning of a gene bearing missense mutations in early-onset familial Alzheimer's disease. Nature *375*, 754–760.

35. Levy-Lahad, E., Wasco, W., Poorkaj, P., Romano, D.M., Oshima, J., Pettingell, W.H., Yu, C.E., Jondro, P.D., Schmidt, S.D., Wang, K., et al. (1995). Candidate gene for the chromosome 1 familial Alzheimer's disease locus. Science (80-.). *269*, 973–977. https://doi.org/10.1126/science.7638622.

36. Li, P., Gao, L., Gaba, A., Yu, L., Cui, L., Fan, W., Lim, A.S.P., Bennett, D.A., Buchman, A.S., and Hu, K. (2020). Circadian disturbances in Alzheimer's disease progression: a prospective observational cohort study of community-based older adults. Lancet Heal. Longev. *1*, e96–e105. https://doi.org/10.1016/S2666-7568(20)30015-5.

37. Al-Turk, W., and Al-Dujaili, E.A.S. (2016). Effect of age, gender and exercise on salivary dehydroepiandrosterone circadian rhythm profile in human volunteers. Steroids *106*, 19–25. https://doi.org/10.1016/j.steroids.2015.12.001.

38. Floyd JA, Janisse JJ, Jenuwine ES, Ager JW (2007). Changes in REM-sleep percentage over the adult lifespan. Sleep *30*, 829–836.

39. Rahman, S.A., Gathungu, R.M., Marur, V.R., St. Hilaire, M.A., Scheuermaier, K., Belenky, M., Struble, J.S., Czeisler, C.A., Lockley, S.W., Klerman, E.B., et al. (2023). Age-related changes in circadian regulation of the human plasma lipidome. Commun. Biol. *6*. https://doi.org/10.1038/s42003-023-05102-8.

40. Cirrito, J.R., Yamada, K.A., Finn, M.B., Sloviter, R.S., Bales, K.R., May, P.C., Schoepp, D.D., Paul, S.M., Mennerick, S., and Holtzman, D.M. (2005). Synaptic activity regulates interstitial fluid amyloid-β levels in vivo. Neuron *48*, 913–922. https://doi.org/10.1016/j.neuron.2005.10.028.

41. Kang J E, Lim M M, Bateman R J, Lee J J, Smyth L P, Cirrito J R, Fujiki N, Nishino S, and Holtzman D M (2009). Amyloid-beta dynamics are regulated orexin and the sleep-wake cycle. Science (80-.). *326*.

42. Saito, T., Matsuba, Y., Mihira, N., Takano, J., Nilsson, P., Itohara, S., Iwata, N., and Saido, T.C. (2014). Single App knock-in mouse models of Alzheimer's disease. Nat. Neurosci. *17*, 661–663. https://doi.org/10.1038/nn.3697.

43. Izumo, M., Pejchal, M., Schook, A.C., Lange, R.P., Walisser, J.A., Sato, T.R., Wang, X., Bradfield, C.A., and Takahashi, J.S. (2014). Differential effects of light and feeding on circadian organization of peripheral clocks in a forebrain Bmal1 mutant. Elife *3*. https://doi.org/10.7554/eLife.04617.

44. Vetter, C. (2020). Circadian disruption: What do we actually mean? Eur. J.

Neurosci. *51*, 531–550. https://doi.org/10.1111/ejn.14255.

45. Davidson, A.J., Sellix, M.T., Daniel, J., Yamazaki, S., Menaker, M., and Block, G.D. (2006). Chronic jet-lag increases mortality in aged mice. Curr. Biol. *16*. https://doi.org/10.1016/j.cub.2006.09.058.

46. Nagare, R., Possidente, B., Lagalwar, S., and Figueiro, M.G. (2020). Robust light–dark patterns and reduced amyloid load in an Alzheimer's disease transgenic mouse model. Sci. Rep. *10*. https://doi.org/10.1038/s41598-020-68199-5.

47. Radde, R., Bolmont, T., Kaeser, S.A., Coomaraswamy, J., Lindau, D., Stoltze, L., Calhoun, M.E., Jäggi, F., Wolburg, H., Gengler, S., et al. (2006). Abeta42-driven cerebral amyloidosis in transgenic mice reveals early and robust pathology. EMBO Rep. *7*, 940–946. https://doi.org/10.1038/sj.embor.7400784.

48. Kondratov, R. V., Kondratova, A.A., Gorbacheva, V.Y., Vykhovanets, O. V., and Antoch, M.P. (2006). Early aging and age-related pathologies in mice deficient in BMAL1, the core component of the circadian clock. Genes Dev. *20*, 1868–1873. https://doi.org/10.1101/gad.1432206.

49. Zott B, Simon MM, Hong W, Unger F, Chen-Engerer HJ, Frosch MP, Sakmann B, Walsh DM, Konnerth A. (2019). A vicious cycle of β amyloid−dependent neuronal hyperactivation. Science. *365*, 559–565.

50. Mackenzie, I.R.A., and Miller, L.A. (1994). Senile plaques in temporal lobe epilepsy. Acta Neuropathol. *87*, 504–510. https://doi.org/10.1007/BF00294177.

51. Sheehan, P.W., Nadarajah, C.J., Kanan, M.F., Patterson, J.N., Novotny, B., Lawrence, J.H., King, M.W., Brase, L., Inman, C.E., Yuede, C.M., et al. (2023). An astrocyte BMAL1-BAG3 axis protects against alpha-synuclein and tau pathology. Neuron *111*, 2383-2398.e7. https://doi.org/10.1016/j.neuron.2023.05.006.

52. Yaghouby, F., Donohue, K.D., O'Hara, B.F., and Sunderam, S. (2016). Noninvasive dissection of mouse sleep using a piezoelectric motion sensor. J. Neurosci. Methods *259*, 90–100. https://doi.org/10.1016/j.jneumeth.2015.11.004.

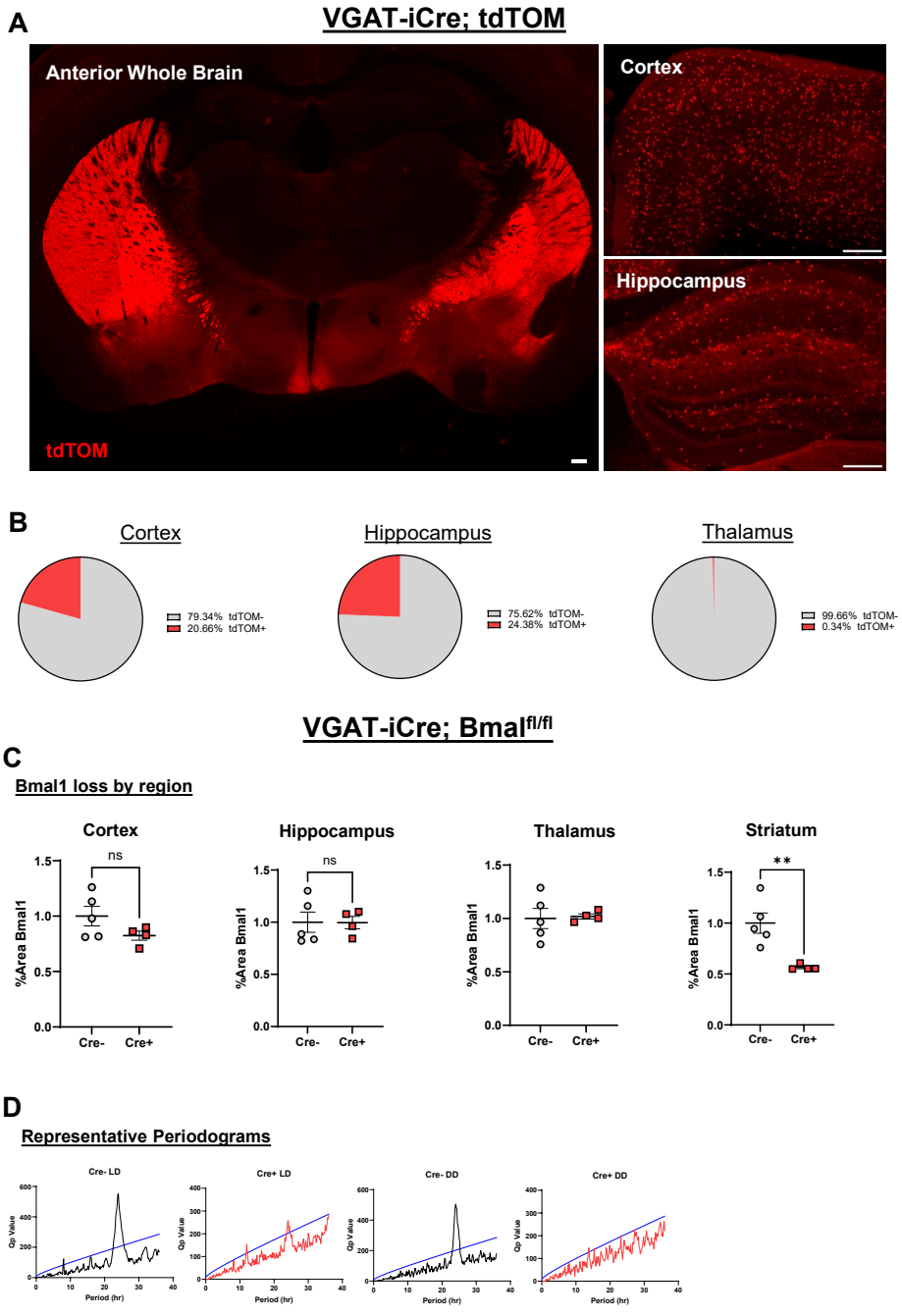

Figure S1.

TdTOM and loss of BMAL1 staining in various regions. **A.** Representative tdTOM fluorescent sections from the anterior whole brain (left), neocortex (upper right) and hippocampus (lower right) of *VGAT-ires-iCre;tdTOM lox-stop-lox* mice. (Scale Bar = 200 μm) **B.** Pie charts of tdTOM+ nuclei among NeuN+ immunostained nuclei from *VGAT-ires-iCre;tdTOM lox-stop-lox* mice (images not shown). **C.** Quantification of Bmal1 loss of immunostaining in selected regions from *VGAT-ires-iCre+;Bmal$^{fl/fl}$* mice. iCre+ mice show a loss of roughly 50% in the striatum (n=4-5 mice per group as indicated, ns: not significant, ** Student's t, $p < 0.005$) **D.** Representative periodograms used to plot the amplitude and period data shown in figures 1E and 1F. Periodograms on the top are LD/periodograms on the bottom are DD.

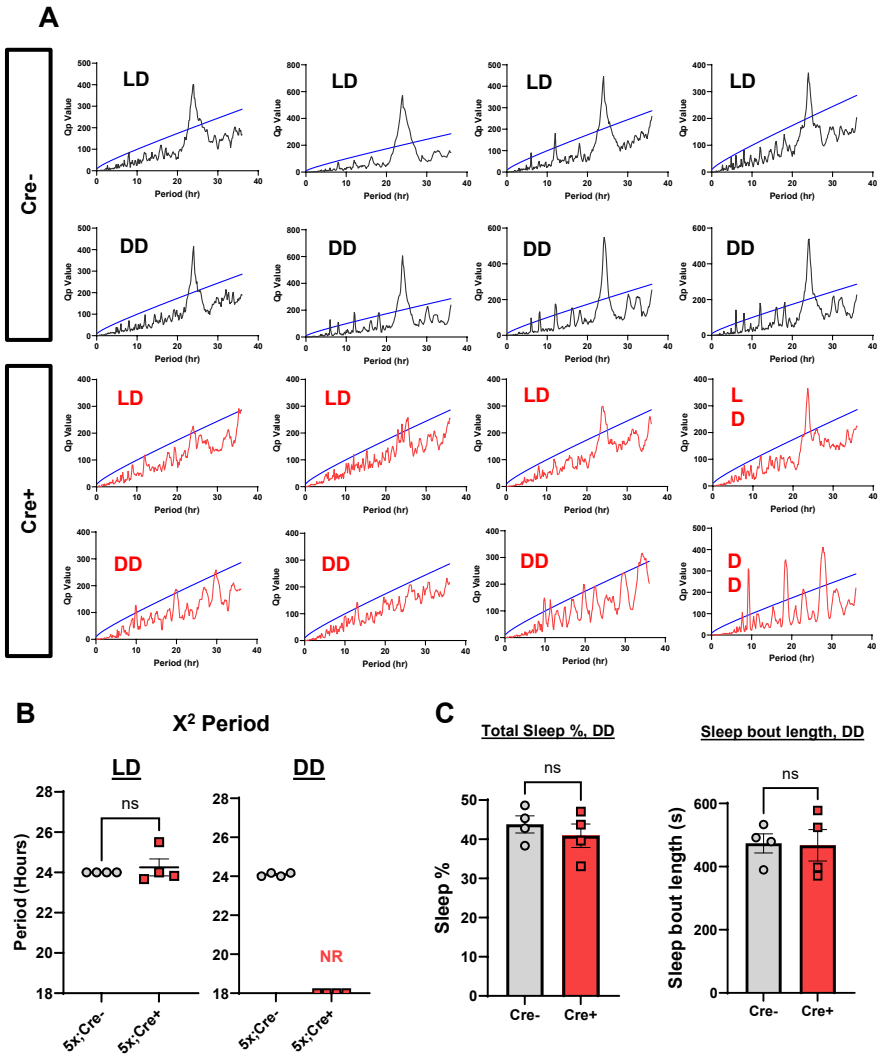

D

Probe	JTK Adj. pval (Cre-)	Adj. pval (Cre+)
Arntl	4.7e-6	0.15
Nr1d1	4.7e-6	0.002
Dbp	2e-6	0.34
Per2	2e-5	0.2
Fabp7	4e-4	1
Nr1d2	0.001	0.26
Cry1	0.002	1
Npas2	0.04	0.06
Cdkn1a	0.63	1

Figure S2

Periodogram, transcriptional, and sleep metrics from GABAergic Bmal1-knockout in 5xFAD mice. **A.** LD and DD periodograms from *VGAT-ires-Cre;Bmal$^{fl/fl}$;5xFAD* mice. **B.** X^2 period analysis quantification from peridograms represented in (A). No coherent rhythms (NR) were seen in Cre+ DD mice. (ns= not statistically significant) **C.** Total Sleep% and Sleep bout length in for *VGAT-ires-Cre;Bmal$^{fl/fl}$;5xFAD* in DD. (ns= not statistically significant) **D.** Table of clock genes and adjusted pvalues as calculated by JTK_CYCLE

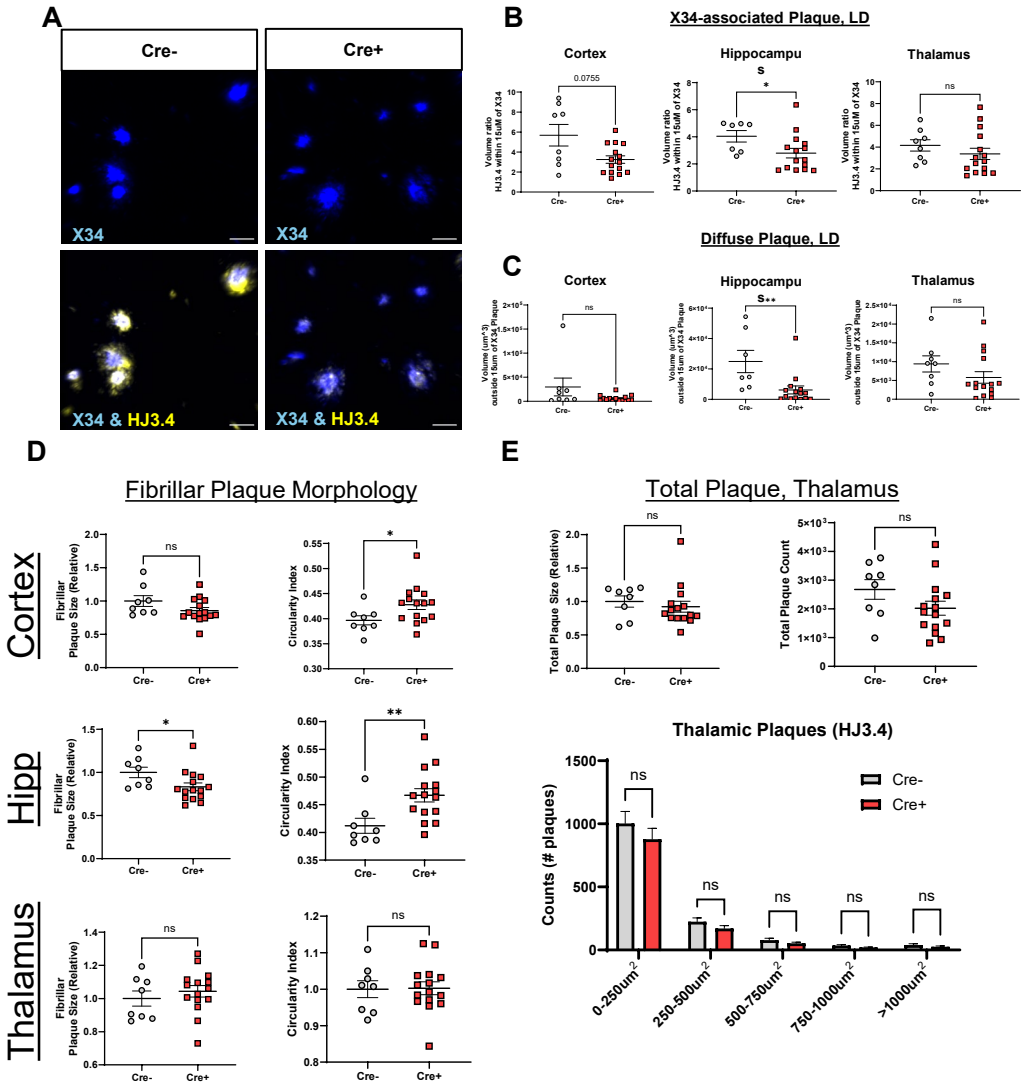

Figure S3

GABAergic BMAL1-knockout alters fibrillar plaque morphology and non-fibrillar plaque aggregation. **A.** Representative confocal images depicting fibrillar (blue, X34) and non-fibrillar (yellow, HJ3.4) Aβ (Scale bar, 20 μm) **B-C** Quantification of peri-plaque HJ3.4 volume generated from 3D surfaces of MIPs depicted in A. All data depicts mean +/- SEM unless otherwise indicated. "X-34 Associated Plaque" denotes HJ3.4 volume within 15 microns of X34 volume. "Diffuse Plaque" denotes HJ3.4 volume outside 15 microns of X34 volume (n=9-15 mice per group as indicated, ns = not statistically significant, p-values between 0.05 and 0.1 are shown, *p < 0.05 by Students t) **D.** Size(first panel) and Circularity Index (second panel) of X34 plaques in selected regions (n=9-15 mice per group as indicated, ns = not statistically significant, *p <0.05 or ** p < 0.005 by Students t) **E.** HJ3.4 Plaque Size, count, and histogram distribution in for the thalamus (n=9-15 mice per group as indicated, ns = not statistically significant)

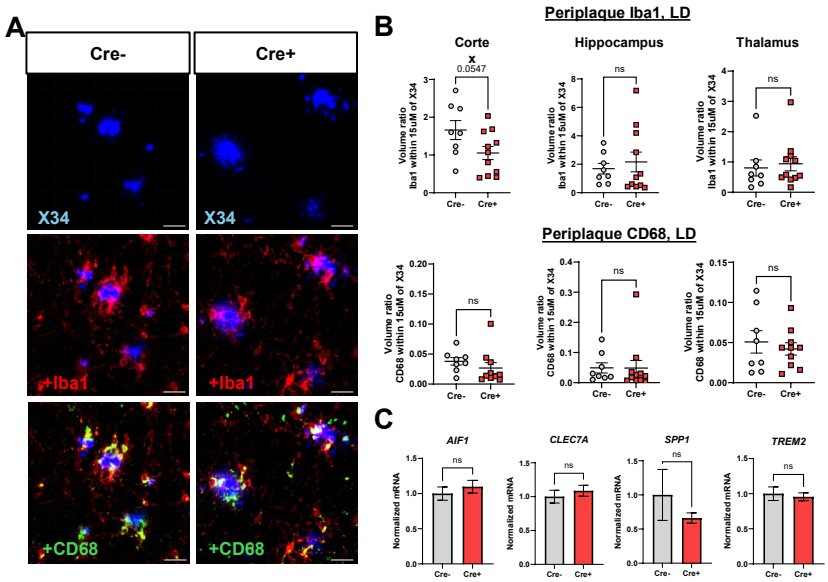

Figure S4

Microglia reactivity and gene expression are unchanged in VGAT-BMAL1 knockout mice. **A.** Representative confocal images depicting fibrillar plaque (blue, X34), Iba1 (red) ad CD68 (green). (Scale bar, 20 µm) **B.** Quantification from (A) Averaged total Iba1 (top) or CD68 (bottom) volume per field divided by X34 volume. (n = 9-15 mice per group, ns=not statistically significant, p-values between 0.05 and 0.1 are displayed) **C.** Bulk hippocampal gene expression using probes against DAM-associated genes. *AIF1*: Allograft Inflammatory Factor 1, *CLEC7a*: C-Type Lectin Domain Containing 7A, SPP1: Secreted Phosphoprotein 1, TREM2: Triggering Receptor Expressed on Myeloid cells 2 (n=9-15 per group as indicated, ns=not statistically significant)

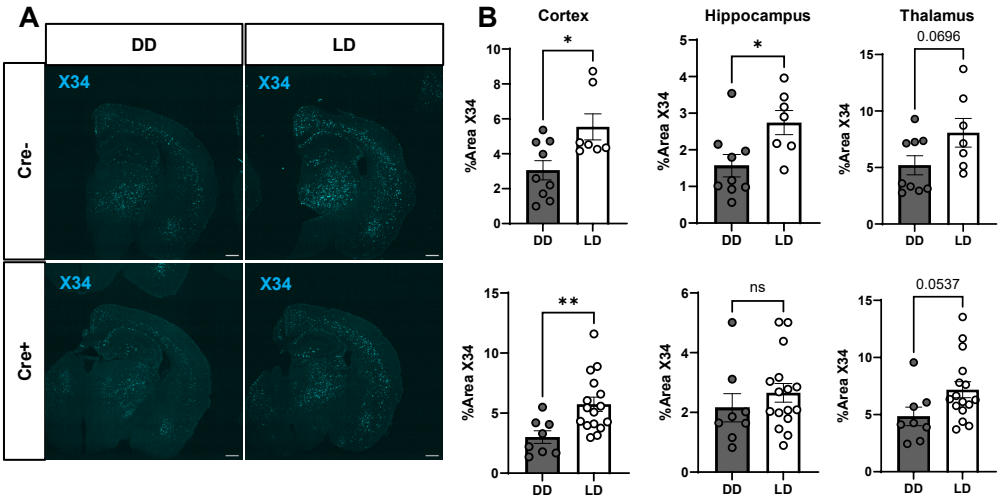

Figure S5

Increased fibrillar plaque aggregation in both VGAT-Cre+ and Cre- LD-treated 5xFAD mice relative to DD. **A.** Representative whole brain images from 5mo *VGAT-ires-Cre;Bmal*$^{fl/fl}$*;5xFAD* mice aged in constant darkness (left) or light-dark (right), depicting staining by X34 (fibrillar plaques, cyan) Scale bar = 500 µm **B.** Quantification from (A) (n = 6-9 mice per group as indicated, *p < 0.05 or **p < 0.005 by Students t, ns = not statistically significant, p-values between 0.05 and 0.1 are displayed

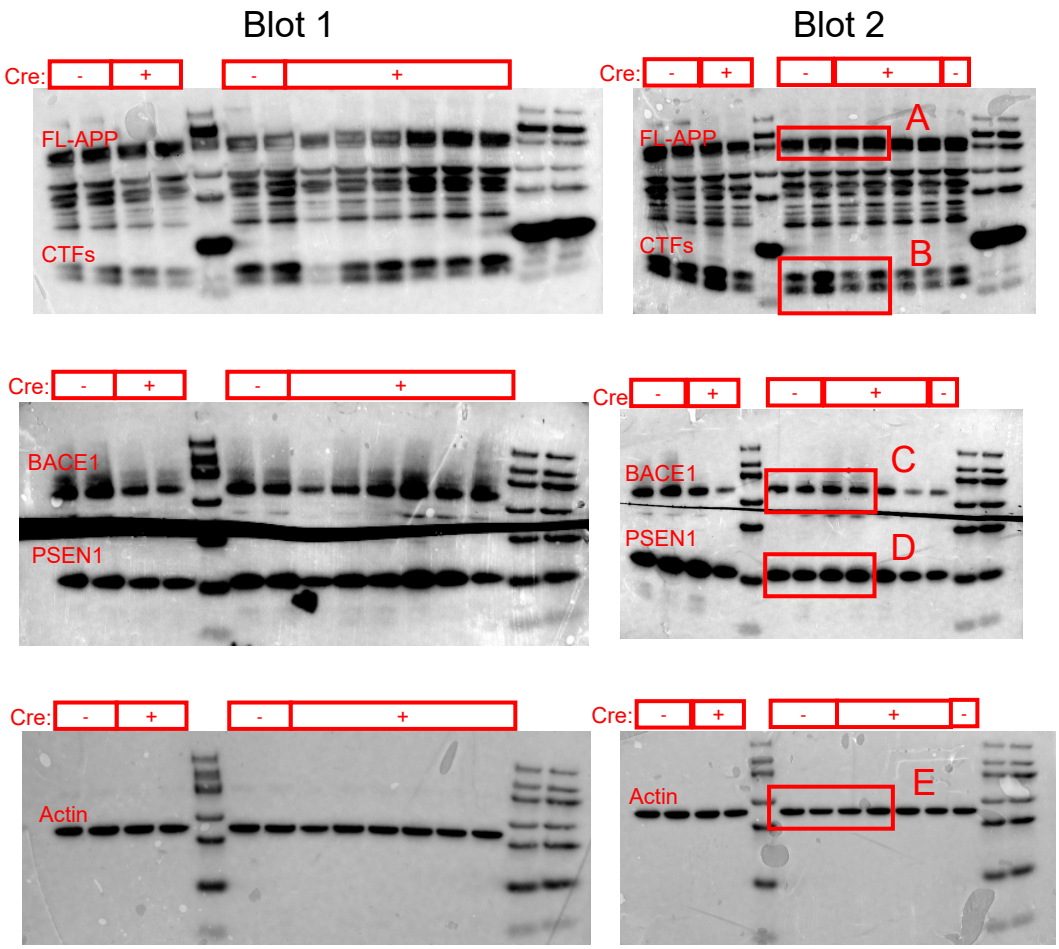

Figure 6B

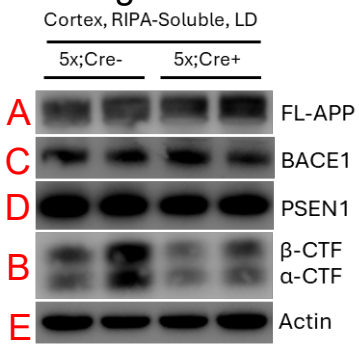

FigureS6

Full immunoblot depicted in Figure 6